Physica Scripta. Vol. 50, 125–134, 1994

Chaotic Electron Trajectories in Quadrupole Wiggler Free Electron Laser

Sinan Bilikmen and Mustafa Abu-Safa

Department of Physics, Middle East Technical University, 06531 Ankara, Turkey

Received July 9, 1993; revised version received January 17, 1994; accepted February 8, 1994

Abstract

The motion of an individual electron in a FEL in a field configuration consisting of an ideal quadrupole-wiggler field and uniform axial-guide field, is shown to be nonintegrable in Hamiltonian formulations and can become chaotic for certain initial conditions. The presence of chaos, which is induced by the transverse spatial inhomogenieties in the wiggler field; and the self-fields produced by the space charge and current, poses limits on the wiggler field amplitude and the beam size for beam propagation in Free-Electron Laser operation. Upon plotting Poincaré surface-of-section maps, it is shown that the electron dynamics is chaotic.

1. Introduction

The Free-Electron Laser (FEL) is a classical device which amplifies short wavelength radiation by stimulated emission using a beam of relativistic electrons, passing through a transverse periodic magnetic field, known as "undulator" or "wiggler".

The undulator may be a helical field, produced by a bifilar helical winding, which will guide the electron along a nearly helical orbit, or it may be a "linearly polarized" field made by a set of alternating polarity magnets. On the other hand the undulator may be an electrostatic device [1]. Usually an axial guide magnetic field is added to confine the electrons against their mutual repulsion.

Theoretical investigations of FEL have been confined, principally, to the linear regime, however, a full nonlinear treatment is required to describe the interaction through the linear stages of saturation [2, 3].

In principle, one can generate a periodic magnetic field by a helical winding of $2l$ wires ($l = 1, 2, \ldots$). A magnetic field of this kind exhibits a helical symmetry and depends on dimensionless coordinates (kr), and ($\phi - kz$). The case $l = 2$ corresponds to a quadrupole magnetic field. This kind of magnetic field requires two pairs of helical windings with current flow in opposite directions in adjacent windings. Moreover, it can be produced by an array of permanent magnets on a circular guide. One can show that the field lines of these kind of fields, are similar to line forces of a quadrupole magnet continuous rotating along the z-axis. A plot of the magnetic surfaces with different mean-radii for the quadrupole magnetic field is shown in Fig. 1.

Recently, an FEL which employs a continuously rotating quadrupole magnetic field as a pump has been suggested. A quadrupole magnetic field is widely used in conventional accelerators as well as in high current accelerators. Lately, quadrupoles have been utilized in ETA/FEL experiment to replace the axial focusing magnetic [4].

Hamiltonian chaos has been an active area of research in physics and applied sciences. The classic work of Kol'mogorov, Arnol'd and Moser (KAM) shows that the generic phase space of nonintegrable classical Hamiltonian systems, subject to small perturbations, contains three types of orbits: stable periodic orbits, stable quasi-periodic orbits (KAM tori), and chaotic orbits [5]. Unlike three-dimensional nonintegrable Hamiltonian systems in which different chaotic regions are isolated by the KAM tori, higher-dimensional, nonintegrable Hamiltonian systems exhibit Arnol'd diffusion behaviour, so that chaotic orbits can reach almost everywhere in phase space. As the perturbation increases in strength, the KAM tori destabilize and become discrete fractal sets. In wave-particle interaction, the breakdown of the last global KAM torus results in stochastic acceleration of particles [6].

It is understood that chaotic behaviour results from strong dependence on initial conditions. If any error develops in time, then nearby trajectories diverge exponentially and the orbit depends sensitively on the initial state. A very small randomness (due to an error of measurement for instance) in the initial state is sufficient for this to occur [7]

The Hamiltonian with N degrees of freedom is integrable if it has N independent constants of motion in involution, e.g. the Poisson bracket of any two of them is zero. If the number of constants is less than N, the motion is nonintegrable and part of the phase space is chaotic in the sense that adjacent initial conditions lead to exponentially divergent trajectories [5, 6, 8]. There are, however, typically

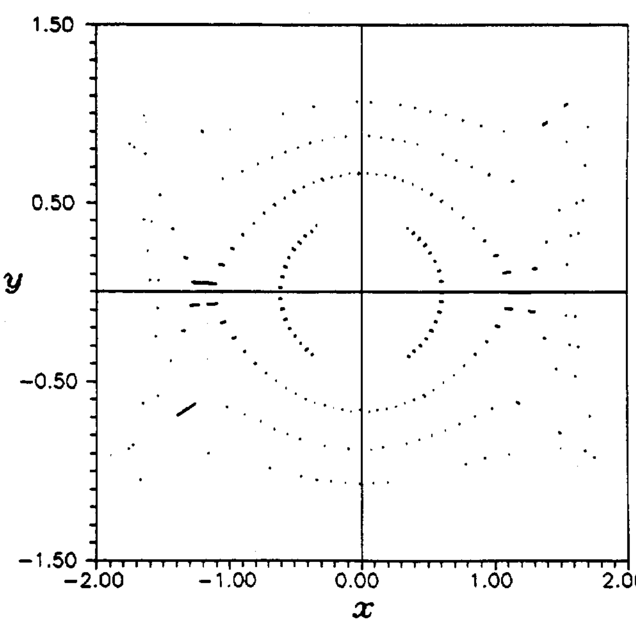

Fig. 1. A plot of the magnetic-surfaces of a quadrupole magnetic field for different mean-radii.

regular regions of phase space as well, the (KAM) surfaces that limit the chaotic parts of phase space.

Earlier investigations of chaos in Free-Electron Lasers have focused on chaotic behaviour in particle orbits induced by sideband and radiation fields. Chen and Schmidt [8], have shown that the electromagnetic signal wave can also cause chaotic electron motion in the combined helical-wiggler and axial-guide field of configuration.

This work examines the motion of relativistic test electron in a quadrupole-wiggler Free-Electron Laser in the absence of electromagnetic signal wave, where the Hamiltonian is found to be nonintegrable, leading to chaotic motion. Of particular interest are the effects of transverse gradients in the beam-self-produced fields and the quadrupole-wiggler field strength on the dynamics of the test electron. To analyse the self-field effects of an intense electron beam, we consider the particle motion in the combined configuration consisting of an ideal (constant-amplitude) quadrupole-wiggler field $\boldsymbol{B}_\omega q$, a uniform axial-guide field $\boldsymbol{B}_0$, and the self-electric and self-magnetic fields produced by space charge and current of the electron beam.

In the limit where self fields are negligibly small, it is found that the onset of chaos for electron orbits occurs whenever the dimensionless parameter $a_\omega = eB_\omega/mc^2k_\omega$ exceeds the critical value a_ω^{cr}. This suggests there is an upper bound on the wiggler field strength for FEL operation.

The chaotic behaviour is demonstrated by generating the Poincaré surface-of-section plots to determine the spread of chaos into the region of phase space where electron beam is located, and then to find the parameter regions for which chaotic behaviour is harmful for the opera of FEL.

The organization of this paper is as follows: In Section 2, a general formulation of the dynamical problem is given, canonical transformations are performed, the problem of integrability is discussed and Hamilton's equations of motion are derived, and the trick of Henón is used to find simply but accurately the intersection of numerically integrated trajectories with surface of section, a computer simulation is developed, and Poincaré surface-of-section plots show the development of chaos by increasing the quadrupole-wiggler field amplitude one time, and increasing the beam density another time and determine the onset of chaos for the system, which is harmful for efficient FEL operation. Finally, Section 3 is left for our comments, conclusions and suggestions for future work.

2. Formulation of the problem

2.1. *Configuration*

One can generate a periodic magnetic field by a helical winding of two pairs of winding, we call this field a quadrupole-wiggler magnetic field because it requires two pairs of helical windings with current flow in opposite directions in adjacent windings. A field of this kind exhibits helical symmetry, i.e. in cylindrical coordinate system the field depends only on the coordinates r and $\theta = \phi - \alpha z$; $\alpha = 2\pi/L$, L is helix pitch. Generally, a second field in the axial direction is added to confine the beam against their natural repulsion. Figure 2 illustrates schematically the quadrupole wiggler configuration. The conductors are wound on the guide tube in a spiral pattern, with currents alternating in direction. The quadrupole wiggler can be pro-

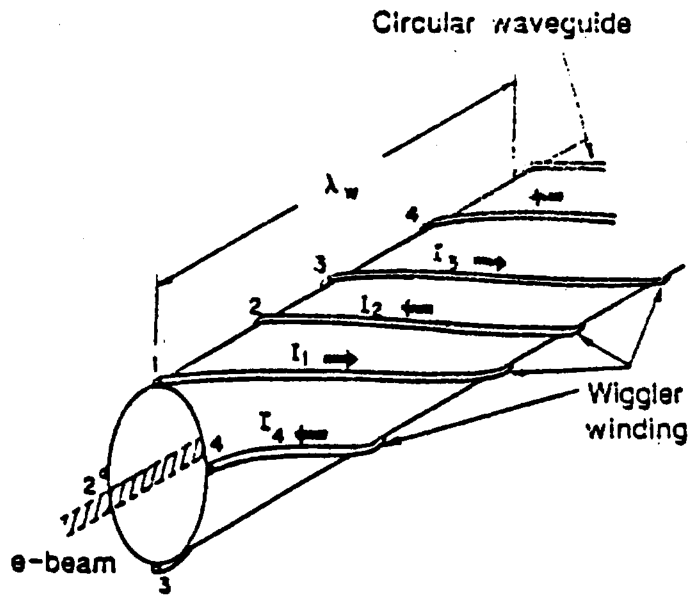

Fig. 2. A FEL configuration with a quadrupole wiggler.

duced by the currents as shown or by an array of permanent magnets on the circular guide which has the advantage of no ohmic dissipation.

The vector potential solution of the static Maxwell equations in vacuum for a helical axial-guide field is in the form [9]

$$A = A_\omega + A_0 = A_r \hat{e}_r + A_\phi \hat{e}_\phi, \tag{1}$$

$$A_r = -\frac{B_\omega}{k_\omega^2 r} I_2(2k_\omega r) \cos 2(\phi - k_\omega z), \tag{2}$$

$$A_\phi = \frac{B_0 r}{2} + \frac{B_\omega}{k_\omega} I_2'(2k_\omega r) \sin 2(\phi - k_\omega z), \tag{3}$$

where B_ω is the wiggler amplitude, $k_\omega = 2\pi/\lambda_\omega$ is the wave number, B_0 is the axial field amplitude, I_2 is the modified Bessel function and I_2' is its derivative.

Then, the static magnetic fields are:

$$B_r = 2B_\omega I_2'(2k_\omega r) \cos 2(\phi - k_\omega z), \tag{4}$$

$$B_\phi = -\frac{2B_\omega}{k_\omega r} I_2(2k_\omega r) \sin 2(\phi - k_\omega z), \tag{5}$$

$$B_z = B_0 + 2B_\omega I_2(2k_\omega r) \sin 2(\phi - k_\omega z). \tag{6}$$

It is readily shown that the wiggler magnetic fields satisfies the vacuum Maxwell equation $\nabla \times \boldsymbol{B}_\omega = 0$. These fields have the form of a right-handed screw in space. Radial plots of these fields were shown in Fig. 3; where the wiggler field goes to zero at $r = 0$.

2.2. *Self-fields*

One of the main purposes of this work is to examine the regular and irregular motion of an individual test electron in the combined applied field configuration and self-fields. In this regard, one has to find the self-electric and self-magnetic fields generated by the beam space charge and current. The electron beam is assumed to have uniform density $n_b(r) = n_0$ and a uniform axial current $j_b = en_0 v_b$ (v_b = const. is the average axial velocity of the beam). It is readily shown from

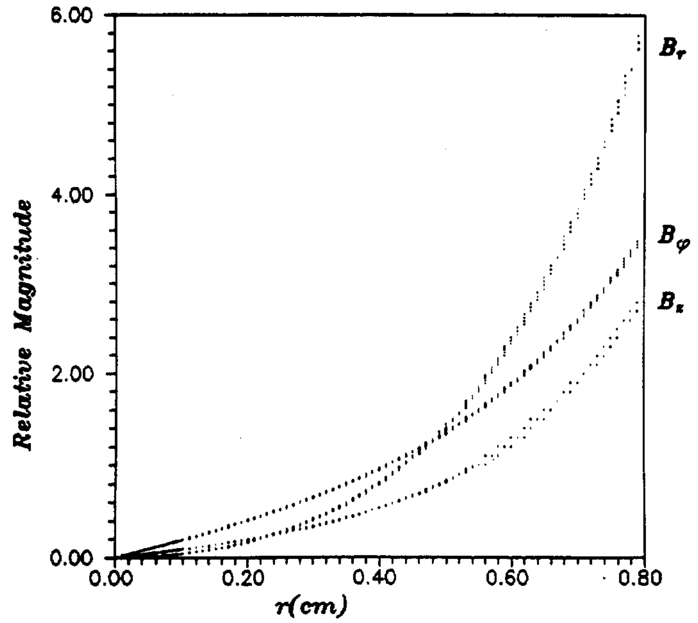

Fig. 3. The radial dependence of the magnetic fields for a quadrupole wiggler.

the steady-state Maxwell equations that [10],

$$E_s = -\frac{m\omega_p^2}{2e}(x\hat{e}_x + y\hat{e}_y), \tag{7}$$

$$B_s = \frac{m\omega_p^2 B_z}{2e}(y\hat{e}_x - x\hat{e}_y) \tag{8}$$

in the beam interior ($0 \leqslant r < r_b$). In eqs (7) and (8), m is the electron rest mass, $\beta_z = v_z/c$, and $\omega_p^2 = (4\pi n_0 e^2/m)$ is the plasma frequency.

It is convenient to represent the self fields as

$$E_s(x) = -\nabla\Phi_s(x), \tag{9}$$

$$B_s(x) = \nabla \times A_s(x), \tag{10}$$

where

$$\Phi_s(x) = \frac{m\omega_p^2}{4e}(x^2 + y^2) = \frac{m\omega_p^2 r^2}{4e}, \tag{11}$$

$$A_s(x) = \beta_z \Phi_s(x)\hat{e}_z. \tag{12}$$

In this sense, the total vector and scalar potentials are given by

$$A(x) = A_0(x) + A_\omega(x) + A_s(x) \tag{13}$$

and

$$\Phi(x) = \Phi_s(x). \tag{14}$$

2.3. *The Hamiltonian representation*

Frequently, equations of motion of the particle can be written quite simply in Hamiltonian form, in which the system of three second-order equations for the coordinates q_i, is represented by a system of six first-order equations for the three coordinates q_i and the three momenta p_i:

$$\frac{dp_i}{dt} = -\frac{\partial H}{\partial q_i}, \tag{15}$$

$$\frac{dq_i}{dt} = \frac{\partial H}{\partial p_i}, \tag{16}$$

which are called the Hamilton's equations of motion, where the relativistic Hamiltonian is given by:

$$H = \{m^2c^4 + [cP + eA]^2\}^{1/2} - e\Phi \equiv \gamma mc^2 - e\Phi_s, \tag{17}$$

where the canonical momentum, P, is related to the mechanical momentum, p, by $P = p - (e/c)A$, and $\gamma = [1 + (p/mc)^2]^{1/2}$ is the relativistic mass factor. Then, the equations of motion for a test electron within the beam $0 \leqslant r < r_b$ can be derived for the Hamiltonian defined in eq. (17), with the vector potential $A(x)$ given in eq. (13). and the electrostatic potential $\Phi_s(x)$ defined in eq. (14).

Because H is independent of time, the Hamiltonian is a constant of motion, i.e.,

$$H = \gamma mc^2 - e\Phi_s = \text{const.} \tag{18}$$

which corresponds to the conservation of total energy (kinetic plus potential energy) of the test electron.

For notational convenience in the subsequent analysis we introduce the dimensionless potentials $\hat{A}(x)$ and $\hat{\Phi}_s(x)$, and Hamiltonian $\hat{H}$ is defined by

$$\hat{A}(x) = \frac{eA(x)}{mc^2}, \quad \hat{\Phi}_s(x) = \frac{e\Phi_s(x)}{mc^2}, \quad \hat{H} = \frac{H}{mc^2}. \tag{19}$$

In addition, the notation

$$a_\omega = \frac{eB_\omega}{mc^2 k_\omega}, \quad a_0 = \frac{eB_0}{mc^2 k_\omega} \tag{20}$$

is introduced, where a_ω is the dimensionless measure of the wiggler field amplitude (B_ω), and a_0 is the dimensionless measure of the axial-guide field (B_0). Because the electric and magnetic self-fields $E_s(x)$ and $B_s(x)$ are proportional to $\omega_p^2 = (4\pi n_0 e^2/m)$ in the beam interior ($0 \leqslant r < r_b$), it is also useful to introduce the dimensionless parameter

$$\varepsilon_s = \frac{\omega_p^2}{c^2 k_\omega^2} \tag{21}$$

which is a measure of the strength of equilibrium self-fields.

Combining eqs (19–(21) with eqs (11), (13) and (17) gives

$$\hat{H} = \left\{1 + \left[\frac{P}{mc} + \hat{A}\right]^2\right\}^{1/2} - \hat{\Phi}_s, \tag{22}$$

where

$$\hat{A}(x) = \frac{a_0 k_\omega r}{2}\hat{e}_\phi + \hat{A}_\omega(x) + \beta_z \hat{\Phi}_s(x)\hat{e}_z, \tag{23}$$

$$\hat{\Phi}_s = \frac{\varepsilon_s k_\omega^2 r^2}{4}. \tag{24}$$

For $k_\omega r < 1$, we expand I_2 to second order in $k_\omega r$ and the normalized wiggler vector potential $\hat{A}_\omega(x)$ becomes

$$\hat{A}(x) = -\frac{a_\omega k_\omega r}{2}\cos 2(\phi - k_\omega z)\hat{e}_r + \frac{a_\omega k_\omega r}{2}\sin 2(\phi - k_\omega z)\hat{e}_\phi, \tag{25}$$

where

$$I_n(n\rho) \cong \frac{1}{n}\left[\frac{n\rho}{2}\right]^n \tag{26}$$

is used for $\rho < 1$. This expansion is used for analytical tractability, and is not used in the computer simulation.

2.4. *Strong pump regime*

The transverse field inhomogeneities in eq. (25) can play an important role in altering the electron motion when the wiggler field amplitude, a_ω, and/or the normalized transverse displacement, $k_\omega r$, becomes sufficiently large [11]. In this section we are interested in the limit where the space charge is negligibly small $\varepsilon_s \to 0$ ($\Phi_s = 0$) and $k_\omega r < 1$, while a_ω is sufficiently large.

In this sense the Hamiltonian is written in the form

$$\hat{H}(k_\omega r, \phi, k_\omega z; \hat{P}_r, \hat{P}_\phi, \hat{P}_z) = \left\{\left[\hat{P}_r - \frac{a_\omega k_\omega r}{2}\cos 2(\phi - k_\omega z)\right]^2 + \left[\frac{\hat{P}_\phi}{k_\omega r} + \frac{a_0 k_\omega r}{2} + \frac{a_\omega k_\omega r}{2}\sin 2(\phi - k_\omega z)\right]^2 + \hat{P}_z^2 + 1\right\}^{1/2}, \tag{27}$$

where

$$\hat{P}_r = \frac{P_r}{mc}, \quad \hat{P}_\phi = \frac{k_\omega P_\phi}{mc}, \quad \hat{P}_z = \frac{P_z}{mc}. \tag{28}$$

In order to an additional constant of motion, it is useful to perform canonical transformations. Because the combination of $(\phi - k_\omega z)$ appears in $\hat{H}$, we perform a canonical transformation to the new variables ($k_\omega r$, χ, $k_\omega z'$; $\hat{P}_r$, $\hat{P}_\chi$, $\hat{P}_{z'}$) defined by [12],

$$k_\omega r = k_\omega r, \quad \chi = \phi - k_\omega z, \quad k_\omega z' = k_\omega z,$$

$$\hat{P}_r = \hat{P}_r, \quad \hat{P}_\chi = \hat{P}_\phi, \quad \hat{P}_{z'} = \hat{P}_z + \hat{P}_\phi. \tag{29}$$

The above transformation was generated by the following generating function:

$$F_2(k_\omega, \phi; \hat{P}_{z'}, \hat{P}_\chi) = k_\omega z \hat{P}_{z'} + (\phi' + k_\omega z)\hat{P}_\chi. \tag{30}$$

Therefore, the Hamiltonian in the new variable can be expressed as

$$\hat{H}(k_\omega r, \chi, k_\omega z'; \hat{P}_r, \hat{P}_\chi, \hat{P}_{z'}) = \left\{\hat{P}_r - \frac{a_\omega k_\omega r}{2}\cos 2\chi\right]^2 + \left[\frac{\hat{P}_\chi}{k_\omega r} + \frac{a_0 k_\omega r}{2} + \frac{a_\omega k_\omega r}{2}\sin 2\chi\right]^2 + [\hat{P}_{z'} - \hat{P}_\chi]^2 + 1\right\}^{1/2}. \tag{31}$$

Because $\hat{H}$ does not depend on $k_\omega z'$, it follows that $\hat{P}_{z'} =$ *const.* Since there is no apparent symmetry to produce a third conservation law, then two constants of motion will not integrate the problem, and the Hamiltonian is nonintegrable. Hence, chaotic orbits are possible. Thus, eq. (31) possesses two constants of motion, namely, $\hat{H}$ and $\hat{P}_{z'}$.

2.5. *Equations of motions*

The Hamilton's equations of motion derived from the Hamiltonian in eq. (31) have the form:

$$\frac{d(k_\omega r)}{d\tau} = \frac{\partial \hat{H}}{\partial \hat{P}_r} = \frac{1}{\gamma}\left[\hat{P}_r - \frac{a_\omega k_\omega r}{2}\cos 2\chi\right], \tag{32}$$

$$\frac{d\chi}{d\tau} = \frac{\partial \hat{H}}{\partial \hat{P}_\chi} = \frac{1}{\gamma}\left\{\frac{1}{k_\omega r}\left[\frac{\hat{P}_\chi}{k_\omega r} + \frac{a_0 k_\omega r}{2} + \frac{a_\omega k_\omega r}{2}\sin 2\chi\right] - [\hat{P}_{z'} - \hat{P}_\chi]\right\}, \tag{33}$$

$$\frac{d\hat{P}_r}{d\tau} = -\frac{\partial \hat{H}}{\partial(k_\omega r)} = -\frac{1}{\gamma}\left\{\left[\hat{P}_r - \frac{a_\omega k_\omega r}{2}\cos 2\chi\right]\left[-\frac{a_\omega}{2}\cos 2\chi\right] + \left[\frac{\hat{P}_\chi}{k_\omega r} + \frac{a_0 k_\omega r}{2} + \frac{a_\omega k_\omega r}{2}\sin 2\chi\right] \times \left[-\frac{\hat{P}_\chi}{k_\omega^2 r^2} + \frac{a_0}{2} + \frac{a_\omega}{2}\sin 2\chi\right]\right\}, \tag{34}$$

$$\frac{d\hat{P}_\chi}{d\tau} = -\frac{\partial \hat{H}}{\partial \chi} = -\frac{1}{\gamma}\left\{\left[\hat{P}_r - \frac{a_\omega k_\omega r}{2}\cos 2\chi\right][a_\omega k_\omega r \sin 2\chi] + \left[\frac{\hat{P}_\chi}{k_\omega r} + \frac{a_0 k_\omega r}{2} + \frac{a_\omega k_\omega r}{2}\sin 2\chi\right] \times [a_\omega k_\omega r \cos 2\chi]\right\}, \tag{35}$$

where, to be consistent, we have used the dimensionless time parameter $\tau = ck_\omega t$.

The fixed points, or the steady-state orbits, denoted by $k_\omega r_0$, χ_0, $\hat{P}_{r0}$ and $\hat{P}_{\chi 0}$, satisfy the steady-state equations of motion

$$\frac{d(k_\omega r)}{d\tau} = 0, \quad \frac{d\chi}{d\tau} = 0, \tag{36}$$

$$\frac{d\hat{P}_r}{d\tau} = 0, \quad \frac{d\hat{P}_\chi}{d\tau} = 0. \tag{37}$$

Hence, substitution of eqs (32)–(35) into these last two yields

$$\left[\hat{P}_{r0} - \frac{a_\omega k_\omega r_0}{2}\cos 2\chi_0\right] = 0, \tag{38}$$

$$\frac{1}{k_\omega r_0}\left[\frac{\hat{P}_{\chi 0}}{k_\omega r_0} + \frac{a_0 k_\omega r_0}{2} + \frac{a_\omega k_\omega r_0}{2}\sin 2\chi_0\right] - [\hat{P}_{z'_0} - \hat{P}_{\chi 0}] = 0, \tag{39}$$

$$\left[-\frac{\hat{P}_{\chi 0}}{k_\omega^2 r_0^2} + \frac{a_0}{2} + \frac{a_\omega}{2}\sin 2\chi_0\right] = 0 \tag{40}$$

$$a_\omega k_\omega r_0 \cos 2\chi_0 = 0. \tag{41}$$

Because $a_\omega \neq 0$ and $k_\omega r_0 \neq 0$, then from eq. (41) we get

$$\cos 2\chi_0 = 0. \tag{42}$$

This leads to

$$\chi_0 = \frac{(2n+1)\pi}{4}; \quad \text{for } n = 0, 1, 2, \ldots \tag{43}$$

Substituting eq. (41) in eq. (38) one gets

$$\hat{P}_{r_0} = 0. \tag{44}$$

and from eq. (40) we get

$$\hat{P}_{\chi 0} = \frac{k_\omega^2 r_0^2}{2}[a_0 \pm a_\omega], \tag{45}$$

where the $\pm$ sign depends on the value of n. Since we assume that in the FEL $a_0 > a_\omega$, it is clear from eq. (45) that the steady-state orbits correspond to a positive normalized angular momentum, i.e.

$$\hat{P}_\phi = \hat{P}_\chi > 0.$$

The radius of the steady-state orbits ($k_\omega r_0$) for a given beam energy, γ_b, is determined from the Hamiltonian in eq. (31), as follows:

$$\hat{H} = \gamma_b = \left\{\left[\frac{\hat{P}_{\chi 0}}{k_\omega r_0} + \frac{a_0 k_\omega r_0}{2} \pm \frac{a_\omega k_\omega r_0}{2}\right]^2 + [\hat{P}_{z'_0} - \hat{P}_{\chi 0}]^2 + 1\right\}^{1/2}. \tag{46}$$

Substituting $\hat{P}_{z'_0}$ from eq. (39) and $\hat{P}_{\chi 0}$ from eq. (45) into eq. (46) yields

$$\gamma_b = \{[a_0 \pm a_\omega]^2 k_\omega^2 r_0^2 + [a_0 \pm a_\omega]^2 + 1\}^{1/2}. \tag{47}$$

Squaring both sides and solving for $k_\omega r_0$ one gets

$$\gamma_b^2 - 1 - [a_0 \pm a_\omega]^2 = [a_0 \pm a_\omega]^2 k_\omega^2 r_0^2 \tag{48}$$

or,

$$k_\omega r_0 = \left\{\frac{\gamma_b^2 - 1 - [a_0 \pm a_\omega]^2}{[a_0 \pm a_\omega]^2}\right\}^{1/2}. \tag{49}$$

In the last equation, all the values of $k_\omega r_0$ are real unless the normalized beam energy γ_b is

$$\gamma_b < \{[a_0 \pm a_\omega]^2 + 1\}^{1/2}. \tag{50}$$

It is, however, more meaningful to plot eq. (49) to represent the real solutions of $k_\omega r_0$. Figure 4 shows $k_\omega r_0$ as a function of the beam energies (γ_b) at the fixed points (steady-state orbits). It is clear that all $\gamma_b > \{[a_0 \pm a_\omega]^2 + 1\}^{1/2}$ yields to bounded orbits.

To check if the problem is integrable or not, we integrate numerically the equations of motion listed in eqs (32)–(35) which were derived from the Hamiltonian defined in eq. (31), then the nonintegrability of the electron motion is demonstrated upon computing the Poincaré maps.

A trick [13] is used to find, simply but very accurately, the intersection of a numerically integrated trajectory with a surface-of-section. The numerical trick and the integration techniques are discussed in details in Section 2.7.

The Poincaré surface-of-section method is useful in analyzing nonintegrable systems because the dimensionality of the Poincaré surface is $M - 1$ if the motion occurs in an M-dimensional phase space. The motion described by the Hamiltonian in eq. (31) occurs in the three-dimensional phase space (χ, $\hat{P}_\chi$, $\hat{P}_r$) because $k_\omega r$ can be determined from the constancy of $\hat{H}$ and $\hat{P}_{z'}$.

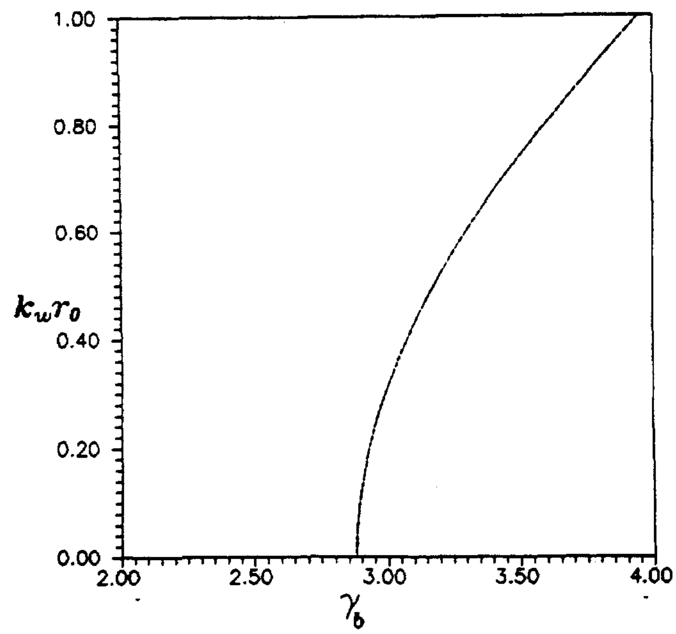

Fig. 4. A plot of $k_\omega r_0$ as a function of the beam energy (γ_b) for the steady-state orbits with $a_0 = 3.0$, and $a_\omega = 0.3$.

As a result, the phase space (χ, $\hat{P}_\chi$) is chosen to be the Poincaré surface-of-section, which demonstrates the regular and chaotic orbits in the vicinity of the steady-state orbits defined in eqs (43)–(45) and eq. (49).

Figure 5 shows the Poincaré surface-of-section plots in the (χ, $\hat{P}_\chi$) plane at $\hat{P}_r = 0$, for $\hat{H} = 3.0$, $a_0 = 3.0$, and $a_\omega = 0.3$. These dimensionless parameters correspond to the $\gamma_b = 3.0$, $B_0 = 10.65$ KG, and $B_\omega = 1.065$ KG for quadrupole wiggler wave length $\lambda_\omega = 3.0$ cm.

It should be pointed out that the contours in Fig. 5 are all on a surface of constant energy, with fixed initial conditions for $k_\omega r$, χ, $\hat{P}_r$, while different initial conditions for $\hat{P}_\chi$ are

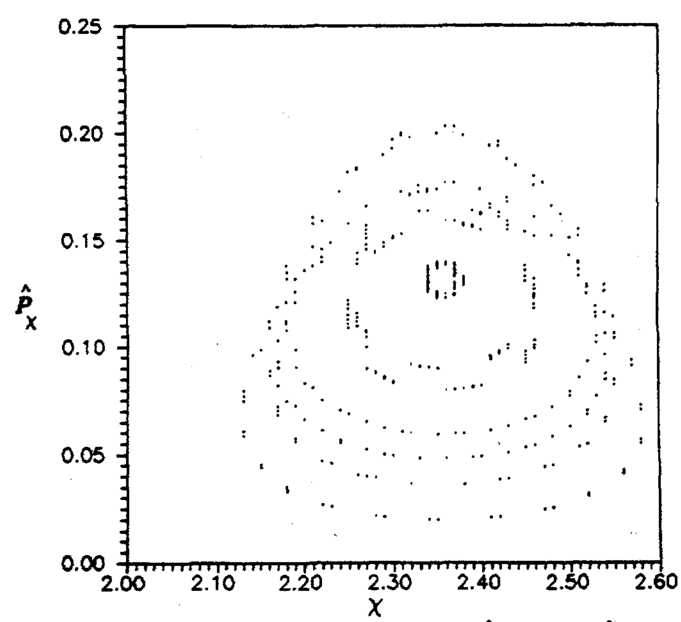

Fig. 5. Poincaré surface-of-section plots in the (χ, $\hat{P}_\chi$) plane at $\hat{P}_r = 0$, for $\hat{H} = 3.0$, $a_0 = 3.0$, and $a_\omega = 0.3$ for different initial conditions of $\hat{P}_\chi$.

accomplished by choosing different values for the canonical axial momentum $\hat{P}_{z'}$. It is evident that these contours present regular trajectories.

An interesting phenomenon is shown in Fig. 6. The stable orbits appear in pairs for a given single initial condition, although this is not the case in the helical wiggler fields of dipole characters. This indicates that the wiggler field we used in our configuration holds its quadrupole characteristics even in phase space. Figure 7 shows the spread of chaos in the Poincaré phase space as the quadrupole wiggler field amplitude is sufficiently large. The figure corresponds to the system parameters $\hat{H} = 3.0$, $a_0 = 3.0$, and $a_\omega = 1.2$. The maximum numerical value for the measure of the wiggler amplitude (a_ω), that reveals regular orbits, is found to be $a_\omega^{cr} = 0.9$ ($B_\omega = 3.20$ KG) in the vicinity of the above selected parameters.

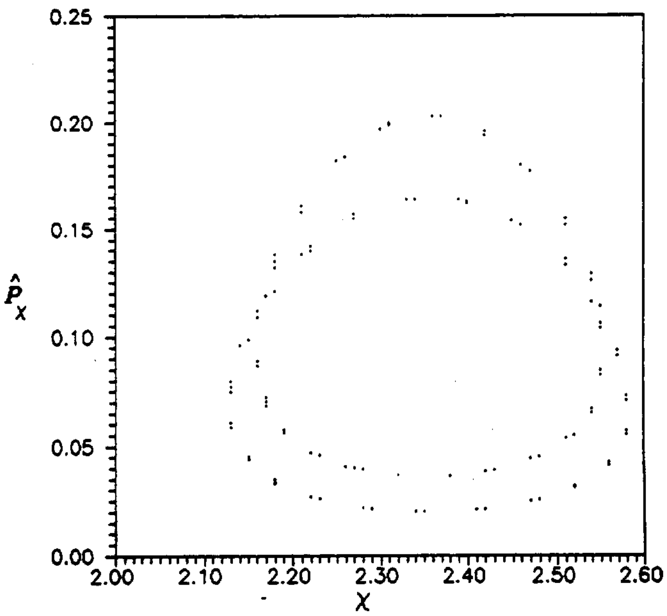

Fig. 6. Poincaré surface-of-section plots in the (χ, $\hat{P}_\chi$) plane at $\hat{P}_r = 0$, for $\hat{H} = 3.0$, $a_0 = 3.0$, and $a_\omega = 0.3$ with only one initial condition.

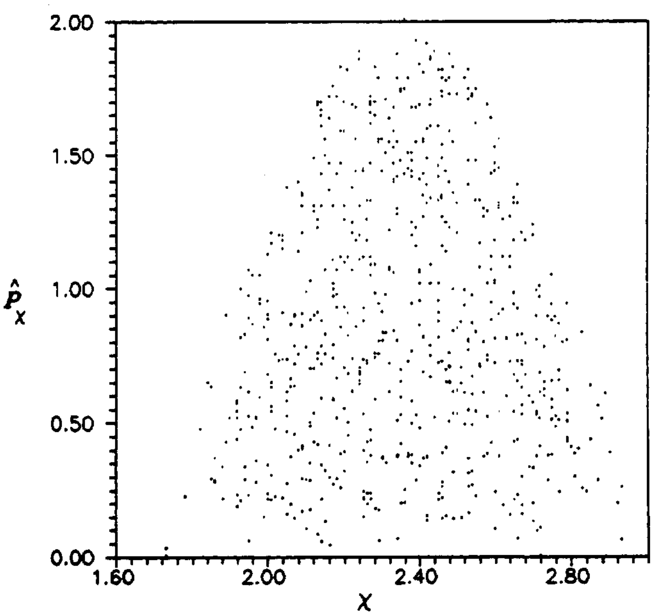

Fig. 7. Chaos in Poincaré surface-of-section plots in the (χ, $\hat{P}_\chi$) plane at $\hat{P}_r = 0$, for $\hat{H} = 3.0$, $a_0 = 3.0$, and $a_\omega = 1.2$ for different initial conditions of $\hat{P}_\chi$.

2.6. *Space charge effect* ($\varepsilon_s \neq 0$)

Free-electron laser operation often requires sufficiently large gain (growth rate), which increases when the beam current is increased. In the high-current (high-density) regime, which is usually called the Raman FEL, the electron motion can be altered significantly by the equilibrium self-field effects associated with the beam space charge and current. This raises important questions regarding beam transport and the viability of the FEL interaction process in this regime.

In this section, our main objective is to show how regular the particle trajectories are once the plasma effects are considered.

Therefore, the motion of a typical test electron within the electron beam can be described by the relativistic Hamiltonian:

$$\hat{H}(k_\omega r, \phi, k_\omega z; \hat{P}_r, \hat{P}_\phi, \hat{P}_z)$$

$$= \left\{1 + \left[\frac{\boldsymbol{P}}{mc} + \hat{A}\right]^2\right\}^{1/2} - \hat{\Phi}_s = \gamma - \hat{\Phi}_s \equiv const.$$

$$= \left\{\left[\hat{P}_r - \frac{a_\omega k_\omega r}{2}\cos 2(\phi - k_\omega z)\right]^2 + \left[\frac{\hat{P}_\phi}{k_\omega r} + \frac{a_0 k_\omega r}{2} + \frac{a_\omega k_\omega r}{2}\sin 2(\phi - k_\omega z)\right]^2 + \left[\hat{P}_z + \frac{\beta_z \varepsilon_s k_\omega^2 r^2}{4}\right]^2 + 1\right\}^{1/2} - \frac{\varepsilon_s k_\omega^2 r^2}{4}. \quad (51)$$

The scalar and the vector potentials related to the space charge and current (used in the above Hamiltonian) are all derived in Section 2.2.

The canonical transformation we performed in the preceding analysis is still valid and the Hamiltonian still possesses two constants of motion. Hence, we rewrite the Hamiltonian given in eq. (51) with the new canonical variables as follows

$$\hat{H}(k_\omega r, \chi, k_\omega z'; \hat{P}_r, \hat{P}_\chi, \hat{P}_{z'})$$

$$= \left\{\left[\hat{P}_r - \frac{a_\omega k_\omega r}{2}\cos 2\chi\right]^2 + \left[\frac{\hat{P}_\chi}{k_\omega r} + \frac{a_0 k_\omega r}{2} + \frac{a_\omega k_\omega r}{2}\sin 2\chi\right]^2 + \left[\hat{P}_{z'} - \hat{P}_\chi + \frac{\beta_z \varepsilon_s k_\omega^2 r^2}{4}\right]^2 + 1\right\}^{1/2} - \frac{\varepsilon_s k_\omega^2 r^2}{4}. \quad (52)$$

It is clear that the two constants of motion are $\hat{H} = const. \neq \gamma$ and $\hat{P}_{z'} = const.$

Here, we represent the corresponding Hamilton's equations of motion as

$$\frac{d(k_\omega r)}{d\tau} = \frac{\partial \hat{H}}{\partial \hat{P}_r} = \frac{1}{\gamma}\left[\hat{P}_r - \frac{a_\omega k_\omega r}{2}\cos 2\chi\right], \quad (53)$$

$$\frac{d\chi}{d\tau} = \frac{\partial \hat{H}}{\partial \hat{P}_\chi} = \frac{1}{\gamma}\left\{\left[\frac{\hat{P}_\chi}{k_\omega r} + \frac{a_0 k_\omega r}{2} + \frac{a_\omega k_\omega r}{2}\sin 2\chi\right]\left[\frac{1}{k_\omega r}\right] - \left[\hat{P}_{z'} - \hat{P}_\chi + \frac{\beta_z \varepsilon_s k_\omega^2 r^2}{4}\right]\right\}, \quad (54)$$

$$\frac{d\hat{P}_r}{d\tau} = -\frac{\partial \hat{H}}{\partial(k_\omega r)}$$
$$= \frac{\varepsilon_s k_\omega r}{2} - \frac{1}{\gamma}\left\{\left[\hat{P}_r - \frac{a_\omega k_\omega r}{2}\cos 2\chi\right]\left[-\frac{a_\omega}{2}\cos 2\chi\right] + \left[\frac{\hat{P}_\chi}{k_\omega r} + \frac{a_0 k_\omega r}{2} + \frac{a_\omega k_\omega r}{2}\sin 2\chi\right] \times \left[\frac{\hat{P}_\chi}{k_\omega^2 r^2} + \frac{a_0}{2} + \frac{a_\omega}{2}\sin 2\chi\right] + \left[\hat{P}_{z'} - \hat{P}_\chi + \frac{\beta_z \varepsilon_s k_\omega^2 r^2}{4}\right]\left[\frac{\beta_z \varepsilon_s k_\omega r}{2}\right]\right\}, \quad (55)$$

$$\frac{d\hat{P}_\chi}{d\tau} = \frac{\partial \hat{H}}{\partial \chi}$$
$$= -\frac{1}{\gamma}\left\{\left[\hat{P}_r - \frac{a_\omega k_\omega r}{2}\cos 2\chi\right][a_\omega k_\omega r \sin 2\chi] + \left[\frac{\hat{P}_\chi}{k_\omega r} + \frac{a_0 k_\omega r}{2} + \frac{a_\omega k_\omega r}{2}\sin 2\chi\right] \times [a_\omega k_\omega r \cos 2\chi]\right\}. \quad (56)$$

Obtaining the equations of motion, we are able to determine the steady-state orbits. Therefore, the fixed points $(k_\omega r_0, \chi_0, \hat{P}_{r0}, \hat{P}_{\chi 0})$ are solutions of the following set of equations:

$$\left[\hat{P}_{r0} - \frac{a_\omega k_\omega r_0}{2}\cos 2\chi_0\right] = 0, \quad (57)$$

$$\left[\frac{\hat{P}_{\chi 0}}{k_\omega r_0} + \frac{a_0 k_\omega r_0}{2} + \frac{a_\omega k_\omega r_0}{2}\sin 2\chi_0\right]\left[\frac{1}{k_\omega r_0}\right] - \left[\hat{P}_{z'0} - \hat{P}_{\chi 0} + \frac{\beta_z \varepsilon_s k_\omega^2 r_0^2}{4}\right] = 0. \quad (58)$$

$$\left\{\left[\frac{\hat{P}_{\chi 0}}{k_\omega r_0} + \frac{a_0 k_\omega r_0}{2} + \frac{a_\omega k_\omega r_0}{2}\sin 2\chi_0\right] \times \left[-\frac{\hat{P}_{\chi 0}}{k_\omega^2 r_0^2} + \frac{a_0}{2} + \frac{a_\omega}{2}\sin 2\chi_0\right] + \left[\hat{P}_{z'0} - \hat{P}_{\chi 0} + \frac{\beta_z \varepsilon_s k_\omega^2 r_0^2}{4}\right] \times \left[\frac{\beta_z \varepsilon_s k_\omega r_0}{2}\right]\right\} - \frac{\gamma(0)\varepsilon_s k_\omega r_0}{2} = 0, \quad (59)$$

$$a_\omega k_\omega r_0 \cos 2\chi_0 = 0. \quad (60)$$

From eq. (60), one finds

$$\chi_0 = \frac{(2n+1)\pi}{4}; \quad \text{for } n = 0, 1, 2, \ldots \quad (61)$$

Substitution of eq. (60) into eq. (57) yields

$$\hat{P}_{r0} = 0. \quad (62)$$

Substituting eqs (57), (58) and (61) in eq. (59), we get

$$\left\{\left[\frac{\hat{P}_{\chi 0}}{k_\omega r_0} + \frac{a_0 k_\omega r_0}{2} \pm \frac{a_\omega k_\omega r_0}{2}\right]\left[-\frac{\hat{P}_{\chi 0}}{k_\omega^2 r_0^2} + \frac{a_0}{2} \pm \frac{a_\omega}{2}\right] + \left[\frac{\hat{P}_{\chi 0}}{k_\omega r_0} + \frac{a_0 k_\omega r_0}{2} \pm \frac{a_\omega k_\omega r_0}{2}\right]\left[\frac{\beta_z \varepsilon_s}{2}\right]\right\} - \frac{\gamma(0)\varepsilon_s k_\omega r_0}{2} = 0, \quad (63)$$

where

$$\gamma(0) \equiv \gamma(k_\omega r_0, \hat{P}_{\chi 0}) = \left\{1 + \left[\frac{\hat{P}_{\chi 0}}{k_\omega r_0} + \frac{a_0 k_\omega r_0}{2} \pm \frac{a_\omega k_\omega r_0}{2}\right]^2 + \left[\frac{\hat{P}_{\chi 0}}{k_\omega r_0} + \frac{a_0 k_\omega r_0}{2} \pm \frac{a_\omega k_\omega r_0}{2}\right]^2\left[\frac{1}{k_\omega^2 r_0^2}\right]\right\}^{1/2}. \quad (64)$$

Making use of the constancy of the Hamiltonian, together with eq. (63) we can determine the radius of the steady-state orbits in the following manner.

For a given beam of electrons with energy E_b, the Hamiltonian in eq. (52) is rewritten as:

$$E = E_b = \gamma(0) - \frac{\varepsilon_s k_\omega^2 r_0^2}{4} = \left\{\left[\frac{\hat{P}_{\chi 0}}{k_\omega r_0} + \frac{a_0 k_\omega r_0}{2} \pm \frac{a_\omega k_\omega r_0}{2}\right]^2\left[1 + \frac{1}{k_\omega^2 r_0^2}\right] + 1\right\}^{1/2} - \frac{\varepsilon_s k_\omega^2 r_0^2}{4}. \quad (65)$$

Solving eq. (65), for $\hat{P}_{\chi 0}$, one gets

$$\hat{P}_{\chi 0} = \frac{k_\omega^2 r_0^2}{2}\left\{2\left[\frac{[E_b + \varepsilon_s k_\omega^2 r_0^2/4]^2 - 1}{k_\omega^2 r_0^2 + 1}\right]^{1/2} - [a_0 \pm a_\omega]\right\}. \quad (66)$$

Now, substitution of $\hat{P}_{\chi 0}$ into eq. (63) yields

$$\frac{\varepsilon_s^2}{4}[E_b + \varepsilon_s k_\omega^2 r_0^2/4]^2[k_\omega^2 r_0^2 + 1]^2 - ([E_b + \varepsilon_s k_\omega^2 r_0^2/4]^2 - 1) \times \left\{[k_\omega^2 r_0^2 + 1]^{1/2}\left[a_0 \pm a_\omega + \frac{\beta_z \varepsilon_s}{2}\right] - ([E_b + \varepsilon_s k_\omega^2 r_0^2/4]^2 - 1)^{1/2}\right\}^2 = 0 \quad (67)$$

By long but simple algebra, the above equation is reduced to the following simple form

$$C_8 X^8 + C_6 X^6 + C_4 X^4 + C_2 X^2 + C_0 = 0, \quad (68)$$

where

$$X = k_\omega r_0, \quad (69)$$

$$C_8 = \left(\frac{3\varepsilon_s^2}{16}\right)^2, \quad (70)$$

$$C_6 = \left[\frac{3\varepsilon_s^2}{8}\right]\left\{\left[\frac{\varepsilon_s^2}{8} + \varepsilon_s E_b\right] - \frac{1}{6}\left[a_0 \pm a_\omega + \frac{\beta_z \varepsilon_s}{2}\right]^2\right\}, \quad (71)$$

$$C_4 = \left(\frac{\varepsilon_s^2}{8} + \varepsilon_s E_b\right)\left\{\left[\frac{\varepsilon_s^2}{8} + \varepsilon_s E_b\right] + \left[\frac{\varepsilon_s E_b}{2} + E_b^2 - 1\right] - \frac{1}{2}\left[a_0 \pm a_\omega + \frac{\beta_z \varepsilon_s}{2}\right]^2\right\} \quad (72)$$

$$C_2 = \left(\frac{\varepsilon_s E_b}{2} + E_b^2 - 1\right)\left\{2\left[\frac{\varepsilon_s^2}{8} + \varepsilon_s E_b\right] - \left[a_0 \pm a_\omega + \frac{\beta_z \varepsilon_s}{2}\right]^2\right\}, \quad (73)$$

$$C_0 = \left\{ \left[\frac{\varepsilon_s E_b}{2} + E_b^2 - 1 \right]^2 - (E_b^2 - 1) \times \left[a_0 \pm a_\omega + \frac{\beta_z \varepsilon_s}{2} \right]^2 \right\}. \quad (74)$$

As one can see from eq. (68) it is of order eight, it is solved numerically for a given set of FEL parameters, namely (a_0, a_ω, β_z, ε_s), and different values of E_b. Four of the eight roots are negative and then neglected, the other four are real and imaginary. The imaginary roots are excluded and some of the real roots are greater than the normalized beam radius ($k_\omega r_b$) and are not considered because of our basic assumption through this section, i.e. ($0 \leqslant r \leqslant r_b$). Thus, we consider the beam energies yielding steady-state orbits with positive, real radius less than the beam radius. Figure 8 shows $k_\omega r_0$ as a function of the beam energies (E_b) at the fixed points (steady-state orbits).

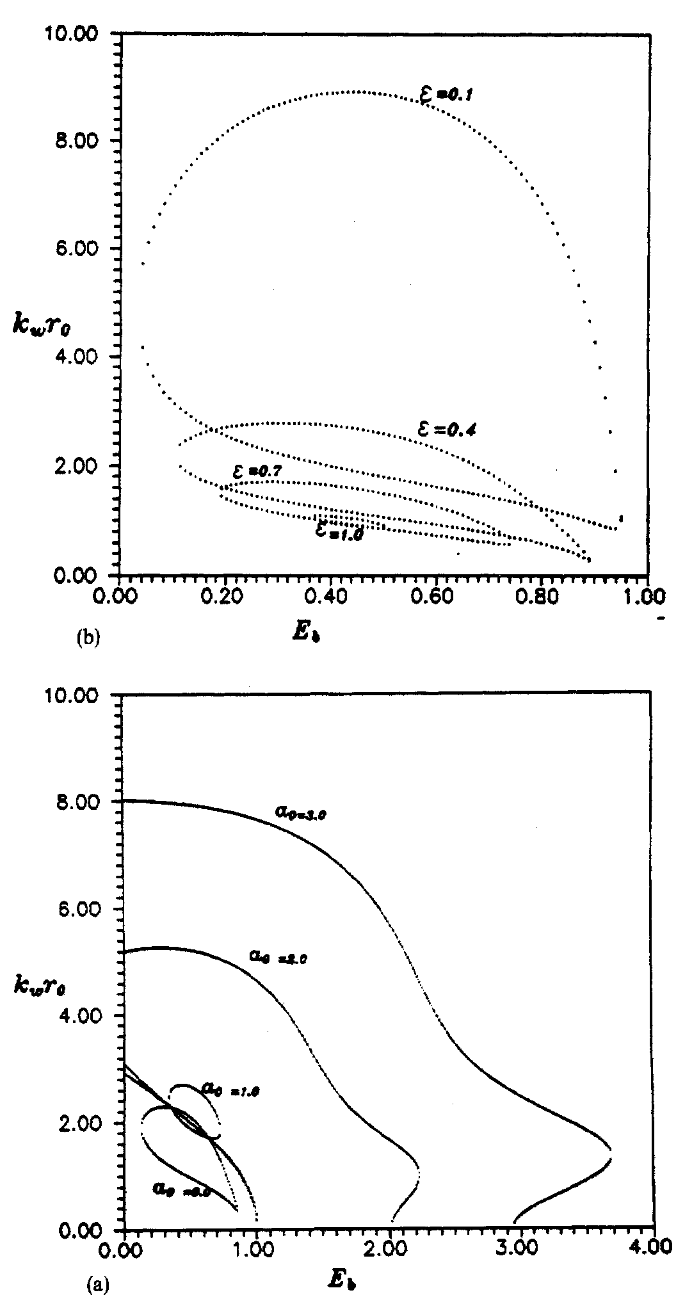

Fig. 8. A plot of $k_\omega r_0$ as a function of the beam energy (E_b) for the steady-state orbits for the two cases: (a) $a_\omega = 0.3$, $\beta_z = 0.94$ and $\varepsilon_s = 0.5$, and (b) $a_0 = 0.0$, $a_\omega = 0.9$, $\beta_z = 0.94$.

It should be pointed out here that, for self convenience, eqs (66) and (67) reduce to eq. (45) and eq. (49) respectively in the limit $\varepsilon = 0$.

Again, to demonstrate the nonintegrability of the system and the chaotic behaviour of the electron trajectories, the Poincaré maps of surface-of-section in phase space are plotted.

Figure 9 shows the stable orbits and the regular electron motion for a low-current (low-density) beam with the dimensionless parameter $\varepsilon_s = 0.5$ for $\hat{H} = 4.00$, $a_0 = 0.0$, $a_\omega = 0.9$, and $\beta_z = 0.94$. Figure 10 shows the unstable orbits and regular electron motion for $\varepsilon_s = 0.5$ for $\hat{H} = 3.00$, $a_0 = 3.0$, $a_\omega = 0.2$, and $\beta_z = 0.94$.

As high-current beams are employed, the phase space regular trajectories are destroyed and chaos spreads strong-

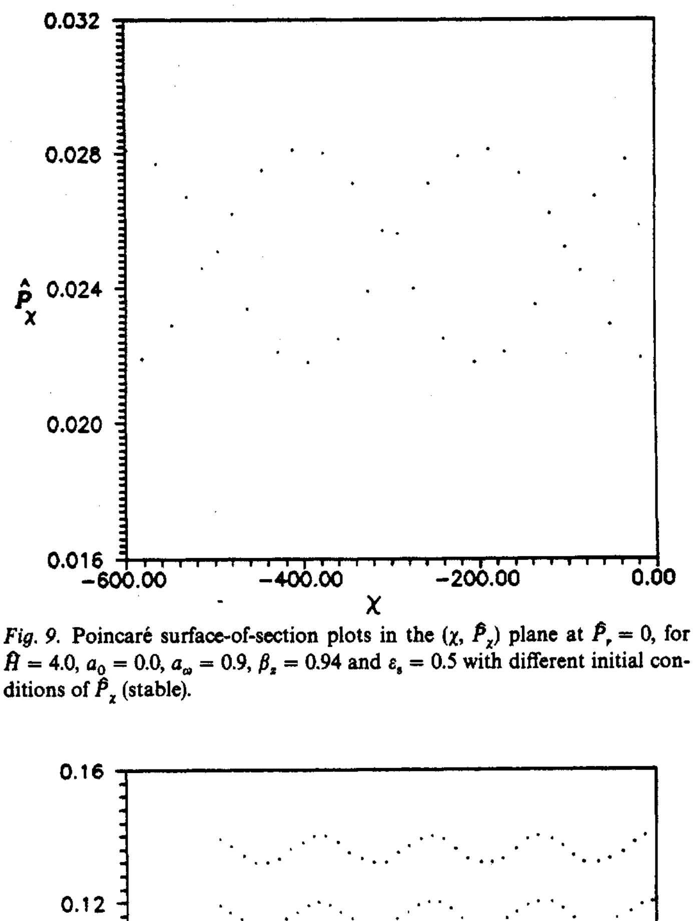

Fig. 9. Poincaré surface-of-section plots in the (χ, $\hat{P}_\chi$) plane at $\hat{P}_r = 0$, for $\hat{H} = 4.0$, $a_0 = 0.0$, $a_\omega = 0.9$, $\beta_z = 0.94$ and $\varepsilon_s = 0.5$ with different initial conditions of $\hat{P}_\chi$ (stable).

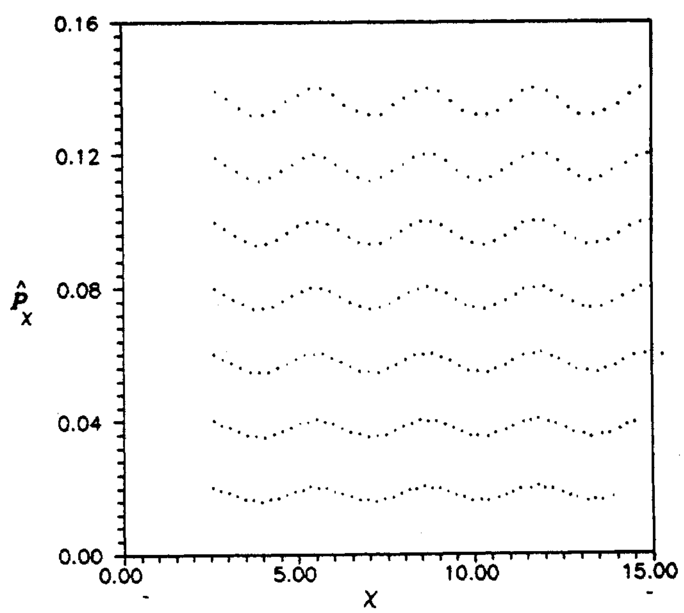

Fig. 10. Poincaré surface-of-section plots in the (χ, $\hat{P}_\chi$) plane at $\hat{P}_r = 0$, for $\hat{H} = 3.0$, $a_0 = 3.0$, $a_\omega = 0.2$, $\beta_z = 0.94$ and $\varepsilon_s = 0.5$ with different initials of $\hat{P}_\chi$ (unstable).

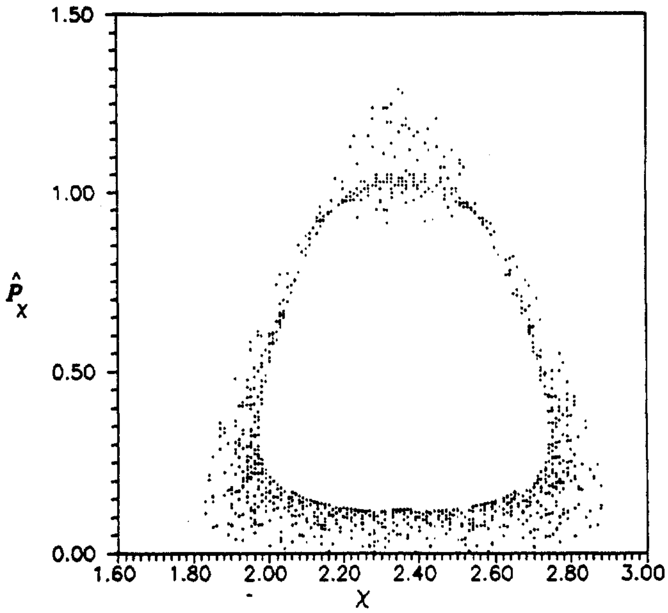

Fig. 11. Chaos in Poincaré surface-of-section plots in the $(\chi, \hat{P}_\chi)$ plane at $\hat{P}_r = 0$, for $\hat{H} = 3.0$, $a_0 = 3.0$, $a_\omega = 0.3$, $\beta_z = 0.94$ and $\varepsilon_s = 1.5$ for different initial conditions of $\hat{P}_\chi$.

ly in Poincaré plots as shown in Fig. 11, which is plotted for $\varepsilon_s = 1.5$ which corresponds to sufficiently large beam density, $n_0 = 1.86 \times 10^{12}\,\text{cm}^{-3}$.

3. Numerical technique and Henòn trick

The numerical computation of the Poincaré surface-of-section maps was improved by using the Henòn trick. We consider an autonomous dynamic system defined by N simultaneous differential equations:

$$\frac{dy_1}{dt} = f_1(y_1, \ldots, y_N),$$
$$\vdots$$
$$\frac{dy_N}{dt} = f_N(y_1, \ldots, y_N). \tag{75}$$

A solution can be represented by a curve, or trajectory, in an N-dimensional phase space $(y_1, \ldots, y_N)$.

The successive intersections of the trajectory with the surface of section Σ, which in general is a $(N-1)$-dimensional subset of phase space, defined by

$$y_i - a = 0, \tag{76}$$

where a is a constant. A problem is that y_i in eq. (76) is a dependent variable; therefore we cannot specify in advance its variation over an integration step. We can simply rearrange the differential system in such a way that y_i becomes an independent variable. This is done by dividing the N equations, excluding the ith one, in system (75), by the ith equation, and inverting the ith one;

$$\frac{dy_1}{dy_i} = \frac{f_1}{f_i},$$
$$\vdots$$
$$\frac{dy_N}{dy_i} = \frac{f_N}{f_i},$$
$$\frac{dt}{dy_i} = \frac{1}{f_i}. \tag{77}$$

Hence, t has now become a dependent variable. The right-hand sides now depend on the independent variable y_i, but this is of no concern.

The practical procedure is as follows. We integrate system (75) until a change of sign is detected for the quantity $S = y_i - a$. We then shift to the system (77). Using the last computed point, we integrate the differential equations in system (77) for one step, taking the integration step

$$\Delta y_N = -S. \tag{78}$$

This brings us at once exactly to the surface of section. After having noted the coordinates of the point, we revert to the system (75) for the continuation of the integration.

4. Results and conclusions

In a Free-Electron Laser, use is made of the unstable interaction of a relativistic electron beam with a transverse wiggler magnetic field to generate coherent electromagnetic waves. An important parameter characterizing FEL operation is the small-signal gain (growth rate). According to linear theory, the gain increases as the beam density and the strength of the wiggler field are increased. However, in the high-current (high-density) regime and in the intense wiggler field (strong-pump) regime, the electron orbit can be modified significantly by the equilibrium self-fields of the electron beams and the transverse spatial gradients in the applied wiggler field. In the high-current (high-density) regime, plasma effects become important, and therefore the self-electric and self-magnetic fields play a significant role in altering the electron dynamics.

In this regard the motion of an inidividual test electron is investigated in the field configuration consisting of a constant amplitude quadrupole wiggler magnetic field, a uniform axial-guide magnetic field, and the equilibrium self-electric and self-magnetic field produced by the non-neutral electron beam.

A Hamiltonian system with N degrees of freedom is integrable if it has N independent constants of motion in involution, e.g., the Poisson bracket of any pair of them is zero. Using this fact, we have formulated the Hamiltonian in canonical variables, and the constants of motion are determined by means of canonical transformations generated by an F_2 kind of generating function. It was found that the Hamiltonian possesses only two independent constants of motion. Thus, it was shown that the motion is nonintegrable and chaotic trajectories became possible.

Here, the nonintegrability is due to the transverse spatial gradients in the applied quadrupole wiggler field. The quadrupole wiggler field is strongly radial dependent and we have demonstrated this fact in Fig. 3.

The Poincaré surface-of-section method is useful in analyzing nonintegrable systems because of the dimensionality of the Poincaré surface is $M-1$ if the motion occurs in an M-dimensional phase space.

The motion described by the Hamiltonians in eqs (31) and (52) occurs in the three-dimensional phase space $(\chi, \hat{P}_\chi, \hat{P}_r)$, because $(k_\omega r)$ is determined from the constancy of $\hat{H}$ and $\hat{P}_{z'}$.

The Poincaré surface-of-section maps have been generated by numerically integrating the equations of motion. This analysis demonstrates the chaotic motion and illustrates that the earlier analytical estimates have captured the underlying physics involved in the nonlinear dynamics of an individual electron.

For the special case where self-field effects are negligibly small, the Poincaré maps of the equations of the motion were generated in Figs 5–7 and 9–11. It was shown that the regular orbits were possible under certain conditions when the quadrupole wiggler amplitude is small. As an example, Fig. 5 shows the phase plane $(\chi, \hat{P}_\chi)$ with quadrupole wiggler field amplitude $a_\omega = 0.3$, is chosen to be the surface-of-section in the numerical calculations to demonstrate the regular trajectories for small quadrupole-wiggler amplitude. It should be pointed out that on the surface of constant energy, with fixed initial conditions of $(k_\omega r, \chi, \hat{P}_r)$, different initial conditions for $\hat{P}_\chi$ are accomplished by choosing different values for the axial canonical momentum $\hat{P}_{z'}$.

When the dimensionless measure of the quadrupole wiggler amplitude (a_ω) is sufficiently large, it was shown that the particle trajectories become strongly chaotic. As the wiggler amplitude is increased, we found that the area of regular region in phase space decreases in the Poincaré surface-of-section plots. A Poincaré map has been created in Fig. 7 showing the chaotic trajectories for $a_\omega = 1.2$. Therefore, this suggests that there is an upper bound on the wiggler field strength for Free-Electron Laser operation.

An interesting feature we mention here is the appearance of closed orbits in the Poincaré surface-of-section for a single initial condition (Fig. 6), while this is not observed in the dipole-wiggler field. In our opinion, this is due to the fact that our wiggler field has quadrupole characteristics.

Second, we have shown that the motion is nonintegrable and becomes chaotic at the dimensionless equilibrium self-field parameter $\varepsilon_s = \omega_p^2/c^2k_\omega^2$ increases in size [here, $\omega_p = (4\pi n_0 e^2/m^2)$ is the plasma frequency]. However, regular trajectories are obtained in the phase space for low-density beam. Although the nonintegrability is evident in the Hamiltonian, and chaotic behaviour is expected, Fig. 9 demonstrates the area of regular region in phase space in the Poincaré surface-of-section for $\varepsilon_s = 0.5$ which corresponds to beam current $I_b = 390\,\mathrm{A}$. That is, the equilibrium self-fields with $\varepsilon_s = 0.5$ are not sufficiently strong to cause significant chaoticity in the particle orbits.

On the other hand, the chaotic behaviour, which is highly increased as the beam current is sufficiently increased, has been shown in Fig. 11 for $\varepsilon_s = 1.5$ which corresponds to a beam current $I_b = 2.34\,\mathrm{kA}$.

In this regard one can say that the existence of chaotic electron orbits places limits on the quadrupole wiggler field amplitude and the transverse beam dimension for beam propagation and Free-Electron Laser operation.

Finally, it should be pointed out that this calculation gives the motion of the electrons in the beam before the signal field builds up to appreciable amplitudes, so that the radiation losses and radiation friction are neglected. It is of our future interests to study the effect of the radiation field on the electron motion in the quadrupole wiggler field configurations, in which the Hamiltonian will be an explicit function of time and hence it is no more a constant of motion.

References

1. Thomas, Marshall C. T., "Free Electron Laser" (Macmillan Publ. Co., 1985), p. 2.
2. Bilikmen, S. and Abu Safa, M., Turkish J. Phys. **16**, 537 (1992).
3. Uddholm, P., Willet, J. E. and Bilikmen, S., J. Phys. **D24**, 1278 (1991).
4. Levush, B., Antonsen, T. M., Manheimer, W. M. and Sprangle, P., Phys. Fluids **28(7)**, 2273 (1985).
5. Sagdeev, R. *et al.*, "Nonlinear Physics from Pendulum to Turbulence and Chaos" (Second Printing) (Harwood Academic Publishers 1990), p. 125.
6. Chen, C. and Davidson, R. C., Phys. Rev. **A43**, 5541 (1991).
7. Hacinliyan, A., Europhys. News **21**, 7 (1991).
8. Chen, C. and Schmidt, G., Comments Plasma Phys. Controlled Fusion **12**, 83 (1988).
9. Chang, S. F., Eldridge, O. C. and Sharer, J. E., IEEE J. of Quantum Electronics **24**, 2308 (1988).
10. Levush, B., Antonsen, T. M. and Manheimer, W. M., J. Apply. Phys. **60**, 1584 (1986).
11. Chen, C. and Davidson, R. C., Phys. Rev. **A42**, 5041 (1990).
12. Goldstein, H., "Classical Mechanics" (Second Edition) (Addison-Wesley 1980), ch. 8.
13. Henòn, M., Physica **5D**, 412 (1982).